Templateless, Plating-Free Fabrication of Flexible Transparent Electrodes with Embedded Silver Mesh by Electric-Field-Driven Microscale 3D Printing and Hybrid Hot Embossing

Xiaoyang Zhu,* Mingyang Liu, Ximeng Qi, Hongke Li, Yuan-Fang Zhang, Zhenghao Li, Zilong Peng, Jianjun Yang, Lei Qian, Quan Xu, Nairui Gou, Jiankang He, Dichen Li, and Hongbo Lan*

Flexible transparent electrodes (FTEs) with an embedded metal mesh are considered a promising alternative to traditional indium tin oxide (ITO) due to their excellent photoelectric performance, surface roughness, and mechanical and environmental stability. However, great challenges remain for achieving simple, cost-effective, and environmentally friendly manufacturing of high-performance FTEs with embedded metal mesh. Herein, a maskless, templateless, and plating-free fabrication technique is proposed for FTEs with embedded silver mesh by combining an electric-field-driven (EFD) microscale 3D printing technique and a newly developed hybrid hot-embossing process. The final fabricated FTE exhibits superior optoelectronic properties with a transmittance of 85.79%, a sheet resistance of 0.75 Ω sq^{-1}, a smooth surface of silver mesh ($R_a \approx 18.8$ nm) without any polishing treatment, and remarkable mechanical stability and environmental adaptability with a negligible increase in sheet resistance under diverse cyclic tests and harsh working conditions (1000 bending cycles, 80 adhesion tests, 120 scratch tests, 100 min ultrasonic test, and 72 h chemical attack). The practical viability of this FTE is successfully demonstrated with a flexible transparent heater applied to deicing. The technique proposed offers a promising fabrication strategy with a cost-effective and environmentally friendly process for high-performance FTE.

Flexible transparent electrodes (FTEs), due to their good mechanical flexibility and photoelectric performance, have attracted enormous attention in recent years in the field of flexible optoelectronics.[1–9] Due to their high optoelectronic performance, transparent conductive oxides, as represented by indium tin oxide (ITO), have been mostly used widely for transparent electrodes (TEs) in the past few decades. However, the inherent properties of ITO such as brittleness and poor flexibility hinder its applications for flexible and stretchable optoelectronic products.[10] Hence, many alternatives to ITO have been developed to address these challenges for the next generation of FTEs, such as graphene,[11] carbon nanotubes,[12,13] conductive polymers,[14–18] transparent thin metal films,[19,20] random metal nanowires,[2,21] regular metal-mesh,[22,23] and hybrid materials.[24,25] Among these FTEs, metal-mesh possesses excellent mechanical flexibility and optoelectronic properties. In particular, the trade-off between low sheet resistance and the high transmittance of TEs can be parametrically designed and further optimized by simply changing the line width, pitch, aspect ratio (AR), shape, and arrangement of the mesh. The metal mesh can be fabricated with a low-cost and large-area manufacturing process (such as solution-process), which can be carried out in a vacuum-free environment and usually requires only a low temperature process.[26–30] So far, FTEs based on metal mesh

Prof. X. Zhu, M. Liu, X. Qi, H. Li, Z. Li, Prof. Z. Peng, Prof. J. Yang, Q. Xu, N. Gou, Prof. H. Lan
Shandong Engineering Research Center for Additive Manufacturing
Qingdao University of Technology
Qingdao 266520, China
E-mail: zhuxiaoyang@qtech.edu.cn; hblan99@126.com
Dr. Y.-F. Zhang
Digital Manufacturing and Design Centre
Singapore University of Technology and Design
Singapore 487372, Singapore

Prof. Z. Peng
College of Engineering
The Ohio State University
Columbus, OH 43210, USA
Dr. L. Qian
Department of Industrial and Systems Engineering
The Hong Kong Polytechnic University
Hung Hom, Hong Kong 999077, China
Prof. J. He, Prof. D. Li
State Key Laboratory for Manufacturing System Engineering
Xi'an Jiaotong University
Xi'an 710049, China

**ADVANCED
SCIENCE NEWS**

www.advancedsciencenews.com

**ADVANCED
MATERIALS**

www.advmat.de

have been used in many fields and have shown broad industrial application prospects.

However, the metal mesh is usually formed on the surface of a flexible transparent substrate, which may easily lead to higher surface roughness, poor adhesion, poor bending fatigue, easy oxidation, and corrosion. Embedded metal mesh can reduce or overcome these defects, and embedded metal mesh provides a new solution for high-performance FTEs. Nonetheless, compared with FTEs with traditional embossed metal mesh, the manufacture of high-performance FTEs with embedded metal mesh faces great challenges. There have been many related studies about fabricating FTEs with embedded metal mesh, especially hybrid manufacturing processes combining various technologies, making the production process complex, costly, and environmentally unfriendly. The candidate technologies mainly include photolithography, laser direct writing, nanoimprinting, electroplating, electroless plating, scraping, cracking, and gravure printing.[31–45] These hybrid manufacturing processes greatly help improve the performance of FTEs with embedded metal mesh. Shen and co-workers demonstrated that silver colloidal nanoparticles could be successfully scraped into the microgrooves fabricated by photolithography or laser direct writing to form embedded metal mesh, and they reached the stage of commercial fabrication.[36,46,47] Li et al. developed a solution-based fabrication approach for FTEs with embedded metal mesh by combining lithography, electroplating, and imprint transfer. The fabricated FTEs with embedded metal mesh showed transmittance (T) higher than 90% and sheet resistance (R_s) below 1 Ω sq^{-1}.[28,48–50] Cui et al. reported a high-performance FTE with a T of 86% and an R_s of 0.03 Ω sq^{-1} using a hybrid printing method that included the imprinting, scraping, and electroplating processes.[42,43] These fabrication strategies for FTEs with embedded metal mesh are all vacuum-free, and the advantages provided by the embedding nature of metal mesh have been verified. According to the literature, mesh-template patterning and metal deposition seem to be the two main processes in the fabrication of embedded metal mesh (Table S1, Supporting information). The mesh-template patterning methods for embedded metal mesh mainly include photolithography, direct laser writing, electron beam lithography, nanoimprint lithography, and the crack method, while the metal deposition methods mainly include the electroplating and electroless plating processes. Most of the template fabrication approaches, such as photolithography and nanoimprint lithography, are costly and complex, and a template with a large area and a high AR is difficult to produce. For most of the fabrication approaches for embedded metal mesh, the plating process is the second critical step because it determines the final performance and the morphology of the embedded metal mesh. However, plating is an environmentally unfriendly process that produces a waste solution and exhaust gas, especially for the electroplating technology. Although several cost-effective fabrication methods for FTEs with embedded metal mesh have been developed based on inkjet printing, electrohydrodynamic jet printing, self-assembly, molding, brush coating, and laser-induced forward transfer,[51–56] the performance of FTEs with embedded metal mesh is still lower than that from the traditional fabrication process. Consequently, a low cost, simple, and environmentally friendly manufacturing method for high-performance FTEs with embedded metal mesh remains a challenge.

In this work, we demonstrated a maskless, templateless, and plating-free fabrication method for high performance FTEs with embedded silver mesh, developed by combining an electric-field-driven (EFD) microscale 3D printing technique and a newly developed hybrid hot-embossing process. First, the EFD microscale 3D printing process was used to fabricate the high-resolution and high-AR silver mesh, and then the silver mesh was embedded into a thermoplastic flexible transparent substrate using a roller-assisted hybrid hot-embossing process to obtain the final FTE. The FTEs with embedded silver mesh produced with this method had the comparable photoelectric properties, mechanical stability, strong adhesion, and chemical reagent corrosion resistance with the FTEs with embedded metal mesh based on the template and electroplating process. Our FTE also exhibited good surface roughness without chemical–mechanical polishing and showed high scratch resistance with a hardness of 3H.

The fabrication procedure of the FTE with embedded silver mesh is explained schematically in **Figure 1**a and clearly shown in Movie S1, Supporting Information. This procedure mainly involved five steps: i) printing the silver paste with high solid content (see Figure S1 and Table S2, Supporting Information) on the hydrophobic treated rigid substrate using the EFD microscale 3D printing process[57] (see Movies S2 and S3, Supporting Information; ii) conductive treating of the embossed silver mesh; iii) laying the transparent flexible poly(ethylene terephthalate) (PET) substrate on the top of the embossed silver mesh using a roller with a positive and negative pressure switchable adsorption tank; iv) embedding the embossed silver mesh into the PET substrate using the roller-assisted hot embossing; and v) separating the FTE with embedded silver mesh from the hard substrate. The FTE with an area of 70 mm × 70 mm and a mesh pitch of 1 mm can be fabricated within an hour, which shows good potential of high manufacturing efficiency comparing with existing fabrication methods of FTEs with embedded metal mesh (Table S3, Supporting information). The structural representation and the images of the final FTE with embedded silver mesh are shown in Figure 1a,b, respectively. Notably, the FTE with embedded silver mesh not only showed good flexible and transparent conductivity, but also showed clearly that the silver mesh was faultlessly embedded within the PET film (see the scanning electron microscopy (SEM) pictures in Figure 1b). More remarkably, due to the smooth contact between the printed embossed silver mesh and the printing substrate, the final FTE with embedded silver mesh could obtain superior surface roughness without any polishing treatment. Figure 1c shows that the surface roughness (R_a) of the FTE within an area of 1 mm² that contained two crossed embedded silver wires was 18.81 nm. In contrast, the surface roughness of the silver wire region (Figure 1d,e) was about 46.6 nm, which was a good result without polishing because the average diameter of the silver nanoparticles in the silver paste was about 200 nm (see Figure S1, Supporting Information).

We demonstrated the novelty and effectiveness of EFD microscale 3D printing in our previous studies.[57–59] In this work, we further prove its potential to produce silver mesh with ultrahigh
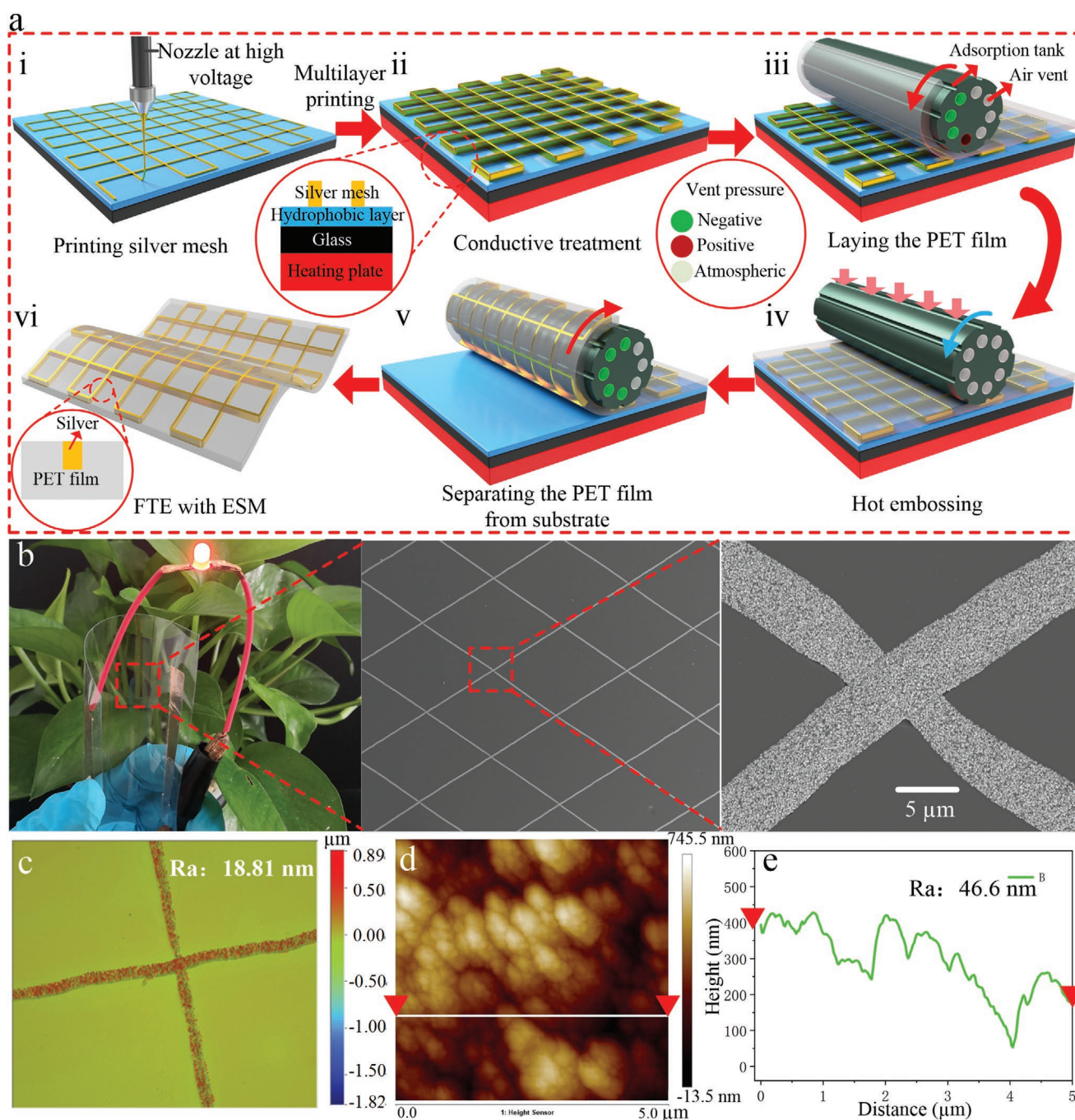
**ADVANCED
SCIENCE NEWS**

www.advancedsciencenews.com

**ADVANCED
MATERIALS**

www.advmat.de

Figure 1. a) A schematic of the fabrication procedure of the FTE with embedded silver mesh. b) The appearance of the FTE and SEM images of the embedded silver mesh. c) The surface roughness of the FTE with an area of 1 mm² measured with a white-light interferometer. d) The surface topography of the surface of the embedded silver mesh with an area of 5 µm² measured by AFM. e) The surface roughness of a cross-sectional surface profile along the segment marked by the two red triangles in (d).

AR and high resolution using a silver paste with high concentration (70 wt%) (see Figures S2 and S3, Movies S2 and S3, Supporting Information). Large-area silver mesh with AR of above 20 can be printed with high efficiency due to the self-excited electrostatic field and the self-aligning effect induced by the charge attraction between the nozzle and the printing silver mesh (see more details in Supporting Information).

Another benefit of our novel fabrication method of FTE is the high-quality imprinting of large-area non-flat, rigid, and fragile silver mesh with high AR based on the hybrid hot embossing, as the roller could be pressed uniformly and stably with low imprinting force and temperature through a linear contact method on the surface of the thermal PET. More importantly, this method can realize a line contact "uncovering-type"

demolding with small and uniform demolding force, allowing a perfect separation between the embedded silver mesh and the original substrate, which is especially suitable for large-scale transfer printing (see Figures S4 and S5 and more details in Supporting Information).

Figure 2 shows the representative SEM images of the printed embossed silver meshes (Figure 2a–c) and the imprinted embedded silver meshes (Figure 2d–f). The partially enlarged details in Figure 2a–c,d–f show the embossed and embedded silver meshes with the number of printed layers being 1–3. These representative SEM images of the embossed and embedded silver meshes show that our new manufacturing strategy can produce FTEs with embedded silver mesh with good morphology and structure. The width of printed embossed silver mesh defined in the diagram in Figure 2k almost remains unchanged with the increase of the number of printed layers (Figure 2j), but the AR of the printed embossed silver mesh gradually increases with the increase of the number of printed layers (Figure 2k). The embossed

silver meshes with the number of printed layers ranging from 1–3 could be embedded into the PET to form a flat top surface with a negligible gap between the PET and the silver surface. During the hot-embossing process, nearly no width change can be found between the embossed silver mesh and the embedded silver mesh (Figure 2l). The cross-sectional SEM images of the embedded silver meshes (Figure 2g–i) also clearly showed that the silver meshes with values of AR ranging from 0.35 to 1 (i.e., number of printed layers from 1 to 3) were completely embedded in the PET substrates. In addition, the embossed silver mesh with an ultrahigh AR of 20 and a line width of 6.5 μm could be successfully fabricated with our EFD microscale 3D printing (Figure S3, Supporting Information). However, when the aspect ratio was greater than 1, defects such as fracturing, collapse, and incomplete encapsulation of embedded silver wires began to appear during the hot-embossing process (Figure S6, Supporting Information). The reason may be that the small imprint force cannot make the silver wire with high AR wrapped completely, while the
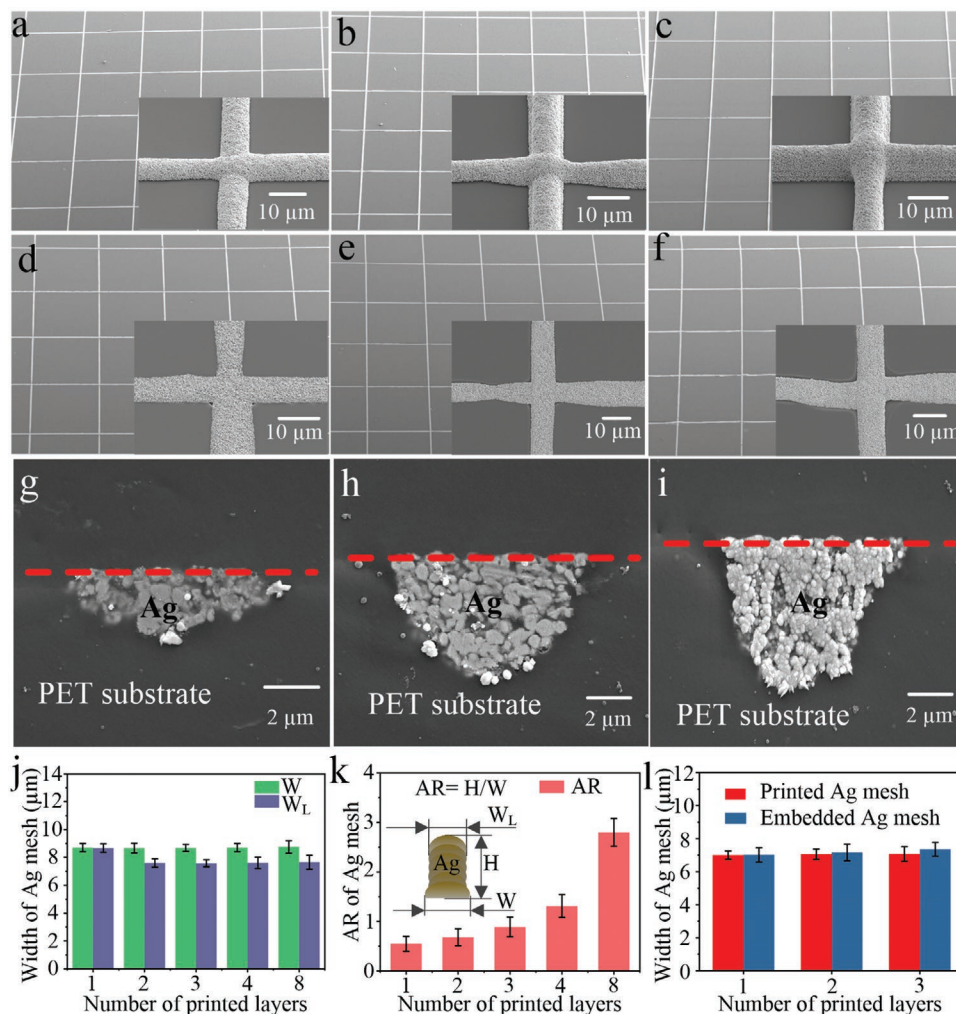

Figure 2. SEM images of the silver meshes. a–c) SEM images of the embossed silver mesh with 1–3 printed layers. d–f) SEM images of embedded silver mesh with 1–3 printed layers. g–i) Cross-sectional SEM images of the embedded silver meshes with values of AR ranging from 0.35 to 1 (i.e., number of printed layers from 1 to 3). j) The relationship between the width of silver mesh and number of printed layers. k) The relationship between the AR of silver mesh and number of printed layers. l) Change of the width of silver mesh before and after hot embossing.

silver wire morphology remains good. Although a large imprint force can make the silver wire wrapped completely, the silver wire will be broken and crushed by the excessive lateral force of the roller (Figures S6–S8, Supporting Information). Therefore, the high yield hot embossing of silver meshes with ultrahigh AR and high resolution might still be a challenge. Furthermore, the novel process can directly fabricate embedded silver meshes with freely designed patterns, such as a rhombus, triangle, or hexagon. (Figure S9, Supporting Information), which is beneficial to the design of optoelectronic devices.

During the microscale 3D printing and hot-embossing process of the silver mesh, the driven voltage of the printing system, printing rate, nozzle driving air pressure, imprinting temperature, and imprinting force were key parameters determining the quality of the FTEs with embedded silver mesh. In order to obtain the printed silver mesh with good surface morphology and the silver mesh embedded completely in PET substrate without fracture and distortion, the optimal parameters are determined experimentally. The results showed that the silver wire had the optimal morphology when the printing voltage was 500–900 V (Figure S10a, Supporting Information) because relatively high or low voltage values might easily make the electric field force and the surface tension of silver paste mismatch, which leads to jet instability. Additionally, the silver wire had the optimal morphology and resolution ratio when the printing rate was 20–40 mm s^{-1} (Figure S10b, Supporting Information). The finer jet is easily affected by the surrounding environment, and the deposition is not accurate enough, so the silver wire is prone to bending deformation under a high printing velocity. The optimal nozzle driving air pressure was 130–150 kPa, and the volume replenishment speed of Taylor cone meniscus under a small air pressure may be less than the deposition speed of jet, which easily leads to uneven width of printed silver wire. (Figure S10c, Supporting Information). The optimal parameters were all determined by keeping the other parameters identical, as different printing parameters may affect each other. The inner diameter of the nozzle was kept at 150 μm, and the distance between the nozzle and the substrate was fixed at 250 μm. Moreover, the line width of the silver line could also change significantly through switching the inner diameter of the nozzles (Figure S11, Supporting Information). The optimal imprinting parameters were the imprinting temperature in the range of 100–120 °C and the imprinting force in the range of 35–40 kgf (Figure S12, Supporting Information). A good encapsulation for silver mesh at low temperature or small imprinting force remains challenge due to the insufficient softening of PET, while the whitening phenomenon of PET at high temperature and breaking or twisting of silver wires under large imprinting force appear, which hinders the improvement of imprint temperature and force (Figure S6, Supporting Information).

Figure 3a–c compares the appearance images of a bare PET substrate (Figure 3a), a rigid substrate with an embossed silver mesh (Figure 3b), and a PET substrate with an embedded silver mesh (Figure 3c). The width and the pitch of the silver meshes were 10 and 1000 μm, respectively. At the normal visual distance of human eyes, there was no obvious difference in the transparency of the three images shown in Figure 3a–c, which indicated that the fabricated embedded silver mesh had good

optical transmittance. As one of the most important indicators, the photoelectric performance of the FTEs could be tuned by adjusting the pitch of the embedded silver meshes (Figure 3d,e), and the measured results showed that the transmittance and sheet resistance of the FTE increased with the pitch (Figure 3d,e). The figure of merit (FoM) was generally used to describe the trade-off between the transmittance and the sheet resistance of the FTE, which could be calculated using Equation (1) below

$$FoM = \frac{188.5}{R_S \left(T_{550nm}^{-1/2} - 1 \right)} \tag{1}$$

where R_s represents the sheet resistance of the metal-mesh and $T_{550\,nm}$ represents the optical transmittance at a wavelength of 550 nm in the FTE.[60,61] Based on the expression, a higher FoM value indicated a more desirable photoelectric performance.

Figure 3f presents the FoM of the FTE with the embedded silver mesh as a function of the number of printed layers (i.e., AR) of embossed silver mesh with a line width and a pitch of 20 and 1000 μm, respectively. Theoretically, the larger the number of printed layers (i.e., AR) was, the larger the FoM would be. However, there was an inflection point for our FTE where the FoM reached a maximum value. This could be due to the large AR (i.e., the number of printed layers increased) leading to a higher probability of the silver mesh fracturing and collapsing during the hot-embossing process (Figure S6, Supporting Information), resulting in an increase in R_s. Additionally, this caused the PET to wrap the silver incompletely, resulting in a decrease in T. Furthermore, the R_s of the silver mesh printed on glass substrate could be greatly reduced due to sintering at high temperature before the mesh was embedded into the PET substrate (Figure S13, Supporting Information), whereas the adhesion between the glass substrate and the silver mesh sintered at high temperature should be optimized for easy demolding of PET with embedded silver mesh from glass substrate (Figures S13 and S14, Supporting Information). We compared the T at 550 nm and the R_s of various FTEs with embedded conductive materials from the literature, as shown in Figure 3g. The FTE with embedded silver mesh produced in this work outperformed most proposed solutions. For the FTEs with embedded metal meshes shown in Table S1, Supporting Information, our silver meshes exhibited an FoM comparable to that of the embedded metal meshes fabricated using traditional template-based or plating processes. In addition, our novel fabrication approach was cost-effective and it had the potential for large-area manufacturing because neither the embossed silver mesh printing nor the hybrid hot-embossing processes imposed excessive equipment, materials, or environmental requirements.

From the perspective of practical application and commercialization potential, in addition to good photoelectric performance, excellent mechanical stability and environmental adaptability are also vitally important indicators for FTEs. **Figure 4**a,b presents the cyclic bending results of FTEs prepared in this work as well as the commercial FTE with ITO/PET film for comparison. Regardless of the number of printed layers (i.e., AR) of the embossed silver meshes, the curves in Figure 4a show the negligible changes of the R_s of the embedded silver
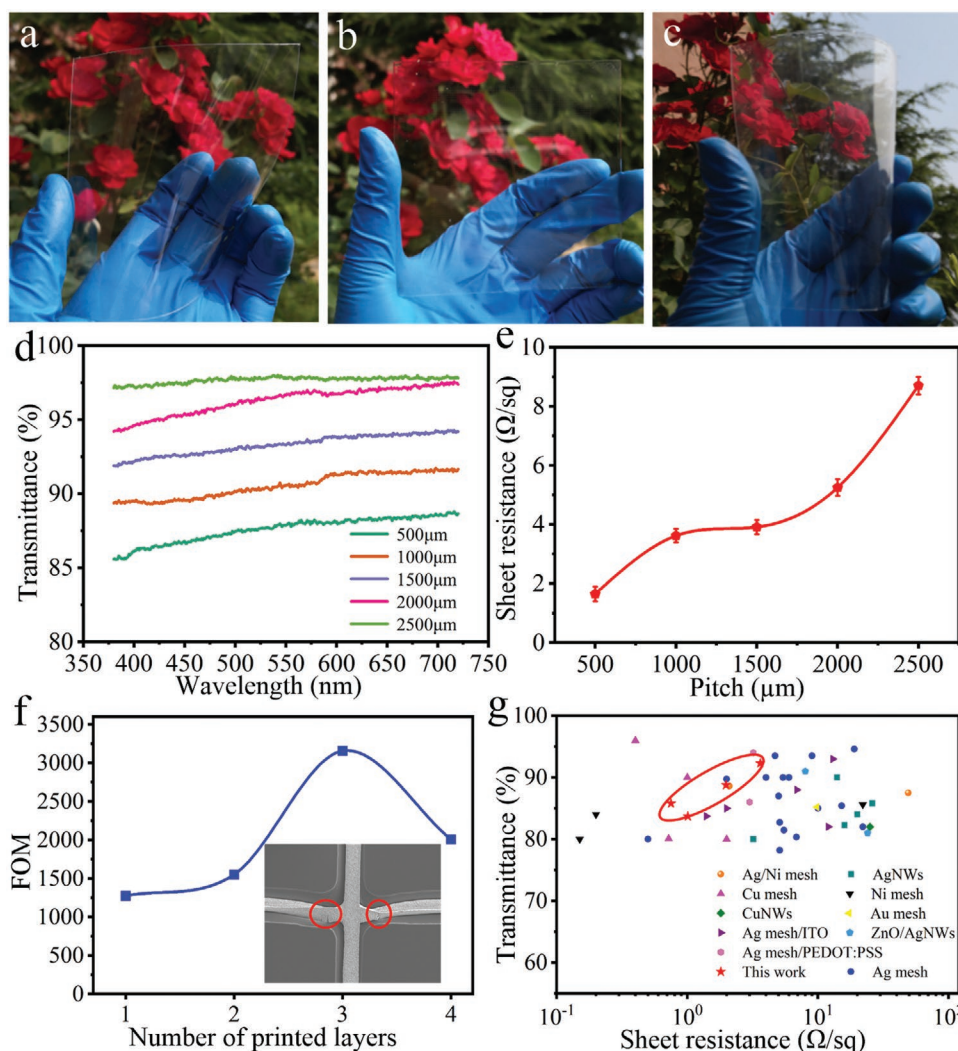
Figure 3. Photoelectric properties of FTE. a) Macroscopic image of the bare PET substrate. b) Macroscopic image of the embossed silver mesh on glass substrate (pitch: 1000 µm, width: 10 µm). c) Macroscopic image of the FTE with embedded silver mesh (pitch: 1000 µm, width: 10 µm). d) Optical transmittance of the embedded silver meshes (width: 15 µm) with different pitch sizes in the visible range. e) Variations in R_s with the pitch of the embedded silver mesh. f) Relationship between the FoM of the embedded silver mesh and the number of printed layers (i.e., AR) of the embossed silver mesh. g) A plot of T at 550 nm as a function of R_s for our FTE with embedded silver mesh and the proposed FTEs with embedded conductive materials.[28,33–37,41,44,50–53,56,62–87]

meshes over 1000 bending cycles with a bending radius of 3 mm (strain: 1.7%, according to refs. [88, 89]), whereas the R_s of the ITO/PET film increased sharply after only 200 bending cycles. Although a larger bending radius (radius: 5 mm, strain: 1%, according to refs. [88, 89]) could improve the mechanical stability of the ITO/PET slightly, the variation of R_s was still significantly larger compared with the proposed embedded silver mesh (Figure 4b). The inset in Figure 4a shows that an LED lamp remained luminous during FTE bending with its brightness essentially unchanged during the bending cycles (Movie S4, Supporting Information). Furthermore, Figure 4g shows that the brightness of a lit LED lamp remained almost constant in a twist state at angles ranging from 90° to 720° (Figure S15 and Movie S5, Supporting Information). The superior bending stability of our FTEs with embedded silver mesh was attributed to their embedded nature and the reduction of the overall FTE film thickness caused by direct embedment in bare PET film.[88]

The mechanical stability of the FTEs with embedded silver mesh could be further verified with repeated adhesion tests of 3M Scotch tape. As shown in Figure 4c, the variation of R_s was less than 3% during 80 peeling tests in the same area, indicating strong adhesion and stability. The hardness and the scratch resistance were essential properties during the practical application of the FTEs because the FTEs needed to have the ability to withstand the possible damage that existed during fabrication and actual usage to ensure a good service life. A pencil test with a pencil hardness of 3H and a pencil tip bearing load of 500 g was used to investigate the hardness and scratch resistance of our FTE in comparison to an embossed silver mesh/PET film and a silver nanowire/PET film. Figure 4d shows that the increase in R_s for the FTE with an embedded silver mesh
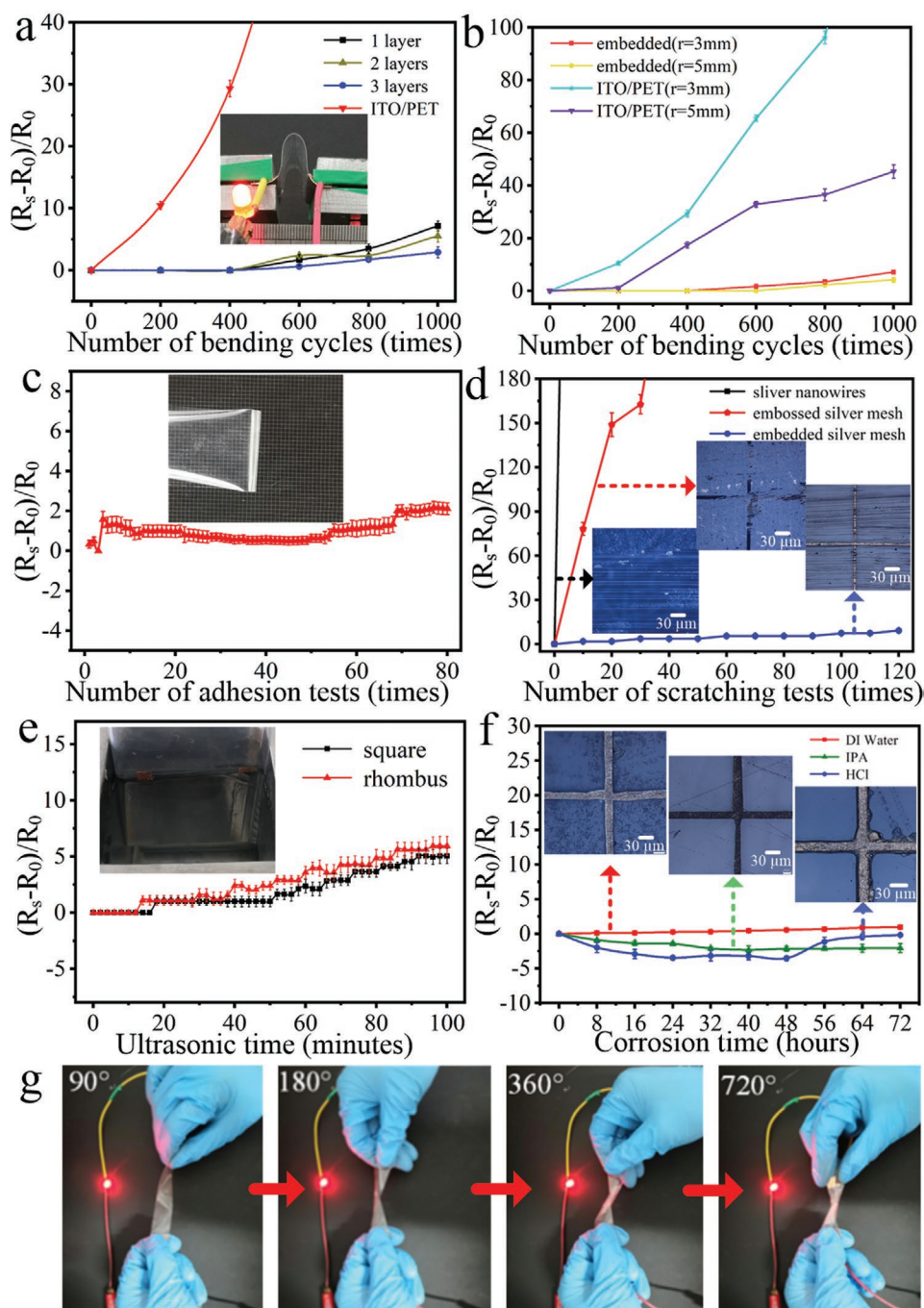
Figure 4. Mechanical stability and environmental adaptability of FTE. a) Comparison of resistance stability of bending between ITO/PET and FET with embedded silver meshes (number of printed layers: 1–3, AR: 0.35–1). b) Comparison of resistance stability of bending between ITO/PET and FET with embedded silver meshes for different bending radii. c) A plot of the relationship between R_s and the number of adhesion tests measured with 3M Scotch tape. d) Comparison of the scratching resistance stability of the embedded silver mesh/PET, embossed silver mesh/PET, and silver nanowire/PET. e) R_s changes for the embedded silver mesh/PET after ultrasonic vibration (30 kHz, 400 W, 50 °C, for 100 min). f) R_s changes for the embedded silver mesh/PET after chemical attack. g) Changes of the brightness for lighting a LED lamp in a twist state at angles ranging from 90° to 720°.

was less than 10% after 120 scratch cycles in the same area, while in comparison, the R_s of the silver nanowire/PET and embossed silver mesh/PET increased several times after a few scratch cycles. In addition, there was nearly no change in the LED brightness during scratching, which could also prove that

our FTE had good scratch resistance (Movie S6, Supporting Information). The surface morphology of the scratched FTEs was studied by optical microscopy; the images are shown in the insets of Figure 4d. For the silver nanowire/PET and embossed silver mesh/PET, the silver nanowire and the embossed wire

**ADVANCED
SCIENCE NEWS**
www.advancedsciencenews.com

**ADVANCED
MATERIALS**
www.advmat.de

in the scraping area were obviously scraped off, while the embedded silver wires in the scraping area were almost unaffected, even if the PET substrate had visible scratches.

To further simulate harsh working conditions, the FTEs with square and rhombus embedded silver meshes were immersed in an ultrasonic water bath (30 kHz, 400 W, 50 °C) to investigate the variation of the R_s of the FTE using ultrasonication. The results of this test are shown in Figure 4e. Only negligible deviations (less than 7%) were observed after the test was performed continuously for a total of 100 min. Figure 4f shows an environmental stability test of the FTE. The FTE was soaked in deionized (DI) water, isopropyl alcohol (IPA), and hydrochloric acid (HCl, pH: 4) solutions to simulate different chemical environment conditions during which the variation of the R_s was collected every 8 h. The results showed no obvious changes in the R_s of the FTE after soaking for 72 h, thus confirming the excellent chemical environment stability of our FTE. The standard damp heat reliability tests (85%, relative humidity (RH) and 85 °C, temperature (T)) were also used to evaluate the stability of our FTE. The results showed only negligible changes in the R_s of our FTE after 3 days, while in comparison, the R_s of the ITO/PET increased significantly (280%) (Figure S16, Supporting Information). Notably, although the surface of embedded silver meshes shown in the insets in Figure 4f and Figure S16c, Supporting Information, were somewhat oxidized and blackened, the R_s of the silver meshes remained almost unchanged because only the surface of the embedded silver meshes were oxidized (Figure S16d, Supporting Information). All of these superior performances of our FTE, including excellent bending and torsion fatigue, adhesion, scratch and vibration resistance, and remarkable chemical corrosion resistance and damp heat reliability, benefited from the good embedding property of silver mesh. Thus, these performance test results indirectly proved that the silver meshes fabricated in this work formed a good embedded structure.

A flexible transparent heater was used to verify the feasibility of our FTE. Transparent electric heating is widely used for demisting and defrosting in wearable electronic devices, display screens, aircraft, automobiles, aerospace equipment, and so forth.[90] For a flexible transparent heater, large-area homogeneous and stable heating, rapid thermal response and cooling rate, and low power consumption are key properties.[91] Figure S17, Supporting Information, shows a schematic diagram of a heating performance test of a flexible transparent heater, in which a pair of contact electrodes that were formed by the silver paste was connected to a DC power supply. The flexible transparent heater with embedded silver mesh was selected as the test sample for the thermal response and cooling rate. The width of the silver wire, the pitch, the AR of the embedded silver mesh, and the mesh pattern area were 20 μm, 1000 μm, 0.3, and 60 mm × 70 mm, respectively. As shown in Figure S18a, Supporting Information, the thermal response and the cooling data were collected by an infrared camera every 10 s. The temperature profiles produced for the DC voltages ranged from 1 to 4 V. The thermal response and the cooling time were ≈150 and 190 s, respectively, independent of the voltage. Figure S18b, Supporting Information, shows a steady-state temperature distribution image for the input voltage of 4 V, thus demonstrating a homogeneous and stable heating performance. Figure S19,

Supporting Information, illustrates the stability of 30 thermal cycles in the flexible transparent heater below 5 V, which proved that our flexible transparent heater had uniform thermal cycling characteristics. However, the maximum heating temperature shown in Figure S19, Supporting Information, was not the steady-state temperature below 5 V because the PET substrate was unable to withstand such a high voltage at the risk of burnout (Figure S20, Supporting Information). To further prove the application effect of electric heating, a flexible transparent heater with embedded silver mesh was selected as the test sample for the deicing. The width of the silver wire, the pitch, the AR of the embedded silver mesh, and the mesh pattern area were 20 μm, 1000 μm, 0.6, and 25 mm × 40 mm, respectively. As shown in Figure S21 and Movie S7, Supporting Information, a piece of ice with a size of 25 × 40 × 3 mm completely melted in 120 s at 3 V voltage, which demonstrated extraordinary electrical heating capabilities. As such, the results presented in this test once again proved that our manufacturing process not only involved no template and no plating process, but also had a low-cost large-area manufacturing capacity. More importantly, the FTE still maintained superior practical performance.

In our future work, the hybrid imprinting technology needs to be further optimized to produce a high-performance FTE with high AR embedded silver mesh. The large-scale parallelization of printing nozzles and the development of conductive paste with short sintering time must be implemented to further improve the manufacturing efficiency and reach the required standard of industrial production. More cost-effective conductive materials, such as copper, should be studied for their printing and hybrid imprinting methods and parameters. The bending fatigue mechanism of embedded silver mesh needs further elaboration, and the trade-off between bending fatigue and photoelectric performance needs to be further studied.

In summary, we have demonstrated a novel simple, cost-effective, and environmentally friendly technology for producing high-performance FTE with embedded silver mesh by combining EFD microscale 3D printing and hybrid hot embossing technology free of the traditional photomask, vacuum deposition, template, and plating processes. The final fabricated FTE exhibited superior optoelectronic properties with a transmittance of 85.79% and a sheet resistance of 0.75 Ω sq^{-1}, which was comparable to the properties produced by template-based or plating-based technologies. Moreover, the thickness of the FTE was effectively reduced by embedding the silver mesh directly in the PET substrate, and the final FTE with embedded silver mesh had superior surface roughness (R_a ≈ 18.8 nm) without any polishing treatment due to the smooth contact between the printed embossed silver mesh and the printing substrate. This novel process could be directly extended to the fabrication of large-area FTE since the EFD microscale 3D printing and hybrid hot embossing are simple and feasible. Our FTE with embedded silver mesh exhibited remarkable mechanical stability and environmental adaptability with a negligible increase in R_s over 1000 bending cycles, 80 adhesion tests, 120 scratch tests, a 100 min ultrasonic test, a 72 h chemical attack using DI water, IPA, and HCl and a standard damp heat reliability tests (RH: 85% and T: 85 °C) for 3 days. Moreover, the practical viability of the proposed FTE was demonstrated based on a successful deicing test via a flexible

transparent heater. These advantages could be attributed to the high-quality embedding of silver mesh in the PET substrate. As such, the fabrication method of the high-performance FTE proposed in this work offers a promising production strategy with a simple, cost-effective, and environmentally friendly process, which paves the way for the low-cost, green, and mass production of a high-performance FTE.

Experimental Section

Materials: The poly(dimethylsiloxane) (PDMS) (Dow Corning SYLGARD 184) curing agent and elastomer were purchased from Dow Corning (USA). The silver paste (NT-TL20E) was purchased from the Beijing Zhongkenatong Electronic Technology Co., LTD (China). The PET was purchased from the Dongguan Dejin Plastic Insulation Material Co., LTD (China). The solvents were purchased from the Shanghai Macklin Biochemical Co., LTD (China).

Fabrication of the FTE with Embedded Silver Mesh: A thin layer of PDMS (ratio of the PDMS elastomer and curing agent: 10:1) was first spin coated on the glass substrate, and a hydrophobic film was formed after curing. Next, the embossed silver mesh with high resolution and high AR was printed on the hydrophobic film using the EFD microscale 3D printing technology, with which the width, pitch, AR, and pattern of the silver mesh could be controlled by adjusting the parameters of the EFD microscale 3D printing. Then the printed embossed silver mesh was conductive treated at 135 °C for 40 min. Subsequently, the embossed silver mesh was transferred and embedded into the PET substrate with a thickness ranging from 25 to 200 μm at a temperature of 100–120 °C via the hybrid hot embossing technology. Finally, the "uncovering-type demolding" was used to separate the FTE with embedded silver mesh from the glass substrate, and to complete the fabrication of the FTE.

Characterization: The silver meshes were cured in an electric blast drying oven at a constant temperature (DHG-903385- III, Shanghai Shengke Instrument Equipment Co., LTD, China). Optical microscopy images of the silver meshes were captured using an optical microscope (DSX510, OLYMPUS, Japan; 3R-MS2020USB, Anyty, China). The process of the EFD microscale 3D printing embossed silver mesh was captured using a digital microscope (Anyty, 3R-MS2020USB, China) and a high-speed camera (i-SPEED221, IX Cameras, UK). The surface roughness of the FTE with embedded silver mesh was determined using a white light interferometer (Veeco Wyko NT9100, USA) and an atomic force microscope (AFM, Dimension Icon, Bruker AXS). The morphology and microscale properties of the silver meshes and silver paste were characterized by field-emission SEM (MERLIN Compact, Zeiss, Germany). Optical transmission of the silver meshes was determined using a UV–vis spectrophotometer (UV-6100, Metash, China) in the wavelength range of 400–800 nm with a step size of 1 nm. The R_s of the silver meshes was measured using a milliohmmeter (AT516, Applent Instruments Co., LTD, China). The analysis of heating performance of the FTE was obtained by infrared camera (TG165, FLIR Systems. USA). The ultrasonic fatigue test of the FTE was demonstrated by ultrasonic cleaner (SCQ-180323P, Shanghai Shengyan Ultrasonic Instrument, China). The bending fatigue test was completed by the self-developed test system. The adhesion test was completed by 3M Scotch tape. The hardness test of the FTE was demonstrated by pencil hardness tester (QHQ-A, Quzhou Aipu Measuring Instrument Co., LTD, China). The standard damp heat reliability tests (RH: 85% and *T*: 85 °C) were completed by temperature and humidity control chamber (SETH-Z-032L, Shanghai ESPEC environmental equipment Co., Ltd, China).

Supporting Information

Supporting Information is available from the Wiley Online Library or from the author.

Conflict of Interest

The authors declare no conflict of interest.

Data Availability Statement

The data that support the findings of this study are available from the corresponding author upon reasonable request.

[1] H. Wu, D. Kong, Z. Ruan, P.-C. Hsu, S. Wang, Z. Yu, T. J. Carney, L. Hu, S. Fan, Y. Cui, *Nat. Nanotechnol.* **2013**, *8*, 421.

[2] C. F. Guo, Z. Ren, *Mater. Today* **2015**, *18*, 143.

[3] D. Li, W. Y. Lai, Y. Z. Zhang, W. Huang, *Adv. Mater.* **2018**, *30*, 1704738.

[4] Y. F. Zhang, N. Zhang, H. Hingorani, N. Ding, D. Wang, C. Yuan, B. Zhang, G. Gu, Q. Ge, *Adv. Funct. Mater.* **2019**, *29*, 1806698.

[5] H. Kim, H. Lee, I. Ha, J. Jung, P. Won, H. Cho, J. Yeo, S. Hong, S. Han, J. Kwon, K. J. Cho, S. H. Ko, *Adv. Funct. Mater.* **2018**, *28*, 1801847.

[6] K. Ellmer, *Nat. Photonics* **2012**, *6*, 809.

[7] K. Yang, S. Chen, J. Fu, S. Jung, J. Ye, Z. Kan, C. Hu, C. Yang, Z. Xiao, S. Lu, K. Sun, *Acs Appl. Mater. Interfaces* **2020**, *12*, 30954.

[8] Y. Xia, K. Sun, J. Ouyang, *Adv. Mater.* **2012**, *24*, 2436.

[9] J. Qin, L. Lan, S. Chen, F. Huang, H. Shi, W. Chen, H. Xia, K. Sun, C. Yang, *Adv. Funct. Mater.* **2020**, *30*, 2002529.

[10] A. Kumar, C. Zhou, *ACS Nano* **2010**, *4*, 11.

[11] Y. Ma, L. Zhi, *Small Methods* **2019**, *3*, 1800199.

[12] I. Jeon, J. Yoon, U. Kim, C. Lee, R. Xiang, A. Shawky, J. Xi, J. Byeon, H. M. Lee, M. Choi, *Adv. Energy Mater.* **2019**, *9*, 1901204.

[13] Y. Zhou, R. Azumi, *Sci. Technol. Adv. Mater.* **2016**, *17*, 493.

[14] H. Shi, C. Liu, Q. Jiang, J. Xu, *Adv. Electron. Mater.* **2015**, *1*, 1500017.

[15] X. Fan, W. Nie, H. Tsai, N. Wang, H. Huang, Y. Cheng, R. Wen, L. Ma, F. Yan, Y. Xia, *Adv. Sci.* **2019**, *6*, 1900813.

[16] L. Zhang, K. Yang, R. Chen, Y. Zhou, S. Chen, Y. Zheng, M. Li, C. Xu, X. Tang, Z. Zang, *Adv. Electron. Mater.* **2020**, *6*, 1900648.

[17] R. Chen, K. Sun, Q. Zhang, Y. Zhou, M. Li, Y. Sun, Z. Wu, Y. Wu, X. Li, J. Xi, *iScience* **2019**, *12*, 66.

[18] Z. Sun, Y. He, B. Xiong, S. Chen, M. Li, Y. Zhou, Y. Zheng, K. Sun, *Angew. Chem.* **2020**, *60*, 5036.

[19] J. Yun, *Adv. Funct. Mater.* **2017**, *27*, 1606641.

[20] C. Ji, D. Liu, C. Zhang, L. J. Guo, *Nat. Commun.* **2020**, *11*, 3367.

[21] T. Sannicolo, M. Lagrange, A. Cabos, C. Celle, J. P. Simonato, D. Bellet, *Small* **2016**, *12*, 6052.

[22] H. B. Lee, W.-Y. Jin, M. M. Ovhal, N. Kumar, J.-W. Kang, *J. Mater. Chem. C.* **2019**, *7*, 1087.

[23] S. Hong, J. Yeo, G. Kim, D. Kim, H. Lee, J. Kwon, H. Lee, P. Lee, S. H. Ko, *ACS Nano* **2013**, *7*, 5024.

[24] R. T. Ginting, M. M. Ovhal, J.-W. Kang, *Nano Energy* **2018**, *53*, 650.

[25] W. Chen, L.-X. Liu, H.-B. Zhang, Z.-Z. Yu, *ACS Nano* **2020**.

[26] J. Schneider, P. Rohner, D. Thureja, M. Schmid, P. Galliker, D. Poulikakos, *Adv. Funct. Mater.* **2016**, *26*, 833.

[27] M. Layani, A. Kamyshny, S. Magdassi, *Nanoscale* **2014**, *6*, 5581.

[28] A. Khan, S. Lee, T. Jang, Z. Xiong, C. Zhang, J. Tang, L. J. Guo, W. D. Li, *Small* **2016**, *12*, 3021.

[29] P. Serra, A. Piqué, *Adv. Mater. Technol.* **2019**, *4*, 1800099.

[30] F. Zacharatos, M. Makrygianni, R. Geremia, E. Biver, D. Karnakis, S. Leyder, D. Puerto, P. Delaporte, I. Zergioti, *Appl. Surf. Sci.* **2016**, *374*, 117.

[31] S. Choi, Y. Zhou, W. Haske, J. W. Shim, C. Fuentes-Hernandez, B. Kippelen, *Org. Electron.* **2015**, *17*, 349.

[32] J. Jang, H.-G. Im, J. Jin, J. Lee, J.-Y. Lee, B.-S. Bae, *ACS Appl. Mater. Interfaces* **2016**, *8*, 27035.

[33] S. Jung, S. Lee, M. Song, D. G. Kim, D. S. You, J. K. Kim, C. S. Kim, T. M. Kim, K. H. Kim, J. J. Kim, *Adv. Energy Mater.* **2014**, *4*, 1300474.

[34] S.-R. Shin, H. B. Lee, W.-Y. Jin, K.-J. Ko, S. Park, S. Yoo, J.-W. Kang, *J. Mater. Chem. C* **2018**, *6*, 5444.

[35] Y. Li, L. Meng, Y. M. Yang, G. Xu, Z. Hong, Q. Chen, J. You, G. Li, Y. Yang, Y. Li, *Nat. Commun.* **2016**, *7*, 10214.

[36] L. Zhou, H.-Y. Xiang, S. Shen, Y.-Q. Li, J.-D. Chen, H.-J. Xie, I. A. Goldthorpe, L.-S. Chen, S.-T. Lee, J.-X. Tang, *ACS Nano* **2014**, *8*, 12796.

[37] S. Han, Y. Chae, J. Y. Kim, Y. Jo, S. S. Lee, S.-H. Kim, K. Woo, S. Jeong, Y. Choi, S. Y. Lee, *J. Mater. Chem. C* **2018**, *6*, 4389.

[38] A. Mahajan, W. J. Hyun, S. B. Walker, J. A. Lewis, L. F. Francis, C. D. Frisbie, *ACS Appl. Mater. Interfaces* **2015**, *7*, 1841.

[39] J. Cai, M. Zhang, Z. Sun, C. Zhang, C. Liang, A. Khan, X. Ning, H. Ge, S.-P. Feng, W.-D. Li, *J. Mater. Chem. C* **2019**, *7*, 4363.

[40] X. Huang, F. Zhang, Y. Liu, J. Leng, *ACS Appl. Mater. Interfaces* **2020**, *12*, 23236.

[41] X. Chen, W. Guo, L. Xie, C. Wei, J. Zhuang, W. Su, Z. Cui, *ACS Appl. Mater. Interfaces* **2017**, *9*, 37048.

[42] X. Chen, S. Nie, W. Guo, F. Fei, W. Su, W. Gu, Z. Cui, *Adv. Electron. Mater.* **2019**, *5*, 1800991.

[43] D.-H. Cho, O. E. Kwon, Y.-S. Park, B. G. Yu, J. Lee, J. Moon, H. Cho, H. Lee, N. S. Cho, *Org. Electron.* **2017**, *50*, 170.

[44] Y.-H. Liu, J.-L. Xu, S. Shen, X.-L. Cai, L.-S. Chen, S.-D. Wang, *J. Mater. Chem. A* **2017**, *5*, 9032.

[45] S. Shen, S.-Y. Chen, D.-Y. Zhang, Y.-H. Liu, *Opt. Express* **2018**, *26*, 27545.

[46] Y. Liu, S. Shen, J. Hu, L. Chen, *Opt. Express* **2016**, *24*, 25774.

[47] J.-L. Xu, Y.-H. Liu, X. Gao, Y. Sun, S. Shen, X. Cai, L. Chen, S.-D. Wang, *ACS Appl. Mater. Interfaces* **2017**, *9*, 27649.

[48] C. Zhang, J. Cai, C. Liang, A. Khan, W. D. Li, *Adv. Funct. Mater.* **2019**, *29*, 1903123.

[49] A. Khan, Y.-T. Huang, T. Miyasaka, M. Ikegami, S.-P. Feng, W.-D. Li, *ACS Appl. Mater. Interfaces* **2017**, *9*, 8083.

[50] C. Zhang, A. Khan, J. Cai, C. Liang, Y. Liu, J. Deng, S. Huang, G. Li, W.-D. Li, *ACS Appl. Mater. Interfaces* **2018**, *10*, 21009.

[51] C. Yang, J. Kim, *Bull. Mater. Sci.* **2018**, *41*, 0003.

[52] Y. Lee, W.-Y. Jin, K. Y. Cho, J.-W. Kang, J. Kim, *J. Mater. Chem. C* **2016**, *4*, 7577.

[53] J. Kang, C.-G. Park, S.-H. Lee, C. Cho, D.-G. Choi, J.-Y. Lee, *Nanoscale* **2016**, *8*, 11217.

[54] D. Y. Choi, Y. S. Oh, D. Han, S. Yoo, H. J. Sung, S. S. Kim, *Adv. Funct. Mater.* **2015**, *25*, 3888.

[55] J.-A. Jeong, H.-K. Kim, J. Kim, *Sol. Energy Mater. Sol. Cells* **2014**, *125*, 113.

[56] C. Floriana, F. Caballero-Lucas, J. Fernández-Pradas, S. Ogier, L. Winchester, D. Karnakis, R. Geremia, R. Artigas, P. Serra, *Appl. Surf. Sci.* **2016**, *37*, 265.

[57] X. Zhu, Q. Xu, H. Li, M. Liu, Z. Li, K. Yang, J. Zhao, L. Qian, Z. Peng, G. Zhang, *Adv. Mater.* **2019**, *31*, 1902479.

[58] X. Zhu, Z. Li, Y. Hu, H. Li, J. Yang, H. Lan, *Opt. Laser Technol.* **2020**, *123*, 105943.

[59] G. Zhang, H. Lan, L. Qian, J. Zhao, F. Wang, *3D Print. Addit. Manuf.* **2020**, *7*, 37.

[60] R. E. Glover III, M. Tinkham, *Phys. Rev.* **1957**, *108*, 243.

[61] G. Haacke, *J. Appl. Phys.* **1976**, *47*, 4086.

[62] H.-D. Um, D. Choi, A. Choi, J. H. Seo, K. Seo, *ACS Nano* **2017**, *11*, 6218.

[63] W.-Y. Jin, R. T. Ginting, K.-J. Ko, J.-W. Kang, *Sci. Rep.* **2016**, *6*, 36475.

[64] Z. Wang, P. Yi, L. Peng, X. Lai, J. Ni, *IEEE Trans. Nanotechnol.* **2017**, *16*, 687.

[65] J.-S. Yu, G. H. Jung, J. Jo, J. S. Kim, J. W. Kim, S.-W. Kwak, J.-L. Lee, I. Kim, D. Kim, *Sol. Energy Mater. Sol. Cells* **2013**, *109*, 142.

[66] J.-L. Xu, Y.-H. Liu, X. Gao, Y. Sun, S. Shen, X. Cai, L. Chen, S.-D. Wang, *ACS Appl. Mater. Interfaces* **2017**, *9*, 27649.

[67] G. Tang, B. Tang, *SN Appl. Sci.* **2020**, *2*, 96.

[68] R. Hokari, K. Kurihara, N. Takada, H. Hiroshima, *Appl. Phys. Lett.* **2017**, *111*, 063107.

[69] C.-H. Chuang, B.-H. Chang, J.-M. Chen, D.-M. Lu, *Micro Nano Lett.* **2016**, *11*, 572.

[70] H.-J. Choi, S. Choo, P.-H. Jung, J.-H. Shin, Y.-D. Kim, H. Lee, *Nanotechnology* **2015**, *26*, 055305.

[71] H. J. Kim, S. H. Lee, J. Lee, E. S. Lee, J. H. Choi, J. H. Jung, J. Y. Jung, D. G. Choi, *Small* **2014**, *10*, 3767.

[72] S. Jang, W.-B. Jung, C. Kim, P. Won, S.-G. Lee, K. M. Cho, M. L. Jin, C. J. An, H.-J. Jeon, S. H. Ko, *Nanoscale* **2016**, *8*, 14257.

[73] Y. S. Oh, D. Y. Choi, H. J. Sung, *RSC Adv.* **2015**, *5*, 64661.

[74] Y. S. Oh, H. Choi, J. Lee, H. Lee, D. Y. Choi, S.-U. Lee, K.-S. Yun, S. Yoo, T.-S. Kim, I. Park, *Sci. Rep.* **2017**, *7*, 8837.

[75] T. Cheng, Y.-Z. Zhang, W.-Y. Lai, Y. Chen, W.-J. Zeng, W. Huang, *J. Mater. Chem. C* **2014**, *2*, 10369.

[76] S. Nam, M. Song, D.-H. Kim, B. Cho, H. M. Lee, J.-D. Kwon, S.-G. Park, K.-S. Nam, Y. Jeong, S.-H. Kwon, *Sci. Rep.* **2014**, *4*, 4788.

[77] H.-G. Im, S. H. Jung, J. Jin, D. Lee, J. Lee, D. Lee, J.-Y. Lee, I.-D. Kim, B.-S. Bae, *ACS Nano* **2014**, *8*, 10973.

[78] S.-M. Park, N.-S. Jang, S.-H. Ha, K. H. Kim, D.-W. Jeong, J. Kim, J. Lee, S. H. Kim, J.-M. Kim, *J. Mater. Chem. C* **2015**, *3*, 8241.

[79] J. H. Cho, D. J. Kang, N.-S. Jang, K.-H. Kim, P. Won, S. H. Ko, J.-M. Kim, *ACS Appl. Mater. Interfaces* **2017**, *9*, 40905.

[80] Z. Zhong, K. Woo, I. Kim, H. Hwang, S. Kwon, Y.-M. Choi, Y. Lee, T.-M. Lee, K. Kim, J. Moon, *Nanoscale* **2016**, *8*, 8995.

[81] P. Li, Y. Zhao, J. Ma, Y. Yang, H. Xu, Y. Liu, *Adv. Mater. Technol.* **2020**, *5*, 1900823.

[82] H.-G. Im, J. Jin, J.-H. Ko, J. Lee, J.-Y. Lee, B.-S. Bae, *Nanoscale* **2014**, *6*, 711.

[83] D. Lee, D.-Y. Youn, Z. Luo, I.-D. Kim, *RSC Adv.* **2016**, *6*, 30331.

[84] H. Zhou, H. Mao, X. Meng, Q. Wang, L. Tan, Y. Chen, *Org. Electron.* **2019**, *75*, 105408.

[85] Y. Liu, S. Shen, L. Chen, Y. Zhou, Y. Ye, Y. Wang, W. Qiao, W. Huang, *Proc. SPIE* **2016**, *10019*.

[86] B. R. Patil, M. Mirsafaei, P. P. Cielecki, A. L. F. Cauduro, J. Fiutowski, H.-G. Rubahn, M. Madsen, *Nanotechnology* **2017**, *28*, 405303.

[87] A. Kim, Y. Won, K. Woo, C.-H. Kim, J. Moon, *ACS Nano* **2013**, *7*, 1081.

[88] S. I. Park, J. H. Ahn, X. Feng, S. Wang, Y. Huang, J. A. Rogers, *Adv. Funct. Mater.* **2008**, *18*, 2673.

[89] D. Kim, S.-H. Kim, J. H. Kim, J.-C. Lee, J.-P. Ahn, S. W. Kim, *Sci. Rep.* **2017**, *7*, 45903.

[90] D. T. Papanastasiou, A. Schultheiss, D. Muñoz-Rojas, C. Celle, A. Carella, J. P. Simonato, D. Bellet, *Adv. Funct. Mater.* **2020**, *30*, 1910225.

[91] Y. F. Zhang, Q. Ge, *Smart Mater. Struct.* **2019**, *28*, 115026.